

Multi-objective optimization of surface texture for the slipper/swash plate interface in EHA pumps

Junhui ZHANG^a, Yining SHEN^a, Minyao GAN^b, Qi SU (✉)^a, Fei LYU^a, Bing XU^a, Yuan CHEN^a

^a State Key Laboratory of Fluid Power and Mechatronic Systems, Zhejiang University, Hangzhou 310027, China

^b Shanghai Marine Equipment Research Institute, Shanghai 200031, China

✉ Corresponding author. E-mail: suqi@zju.edu.cn (Qi SU)

© Higher Education Press 2022

ABSTRACT Well-designed surface textures can improve the tribological properties and the efficiency of the electro-hydrostatic actuator (EHA) pump under high-speed and high-pressure conditions. This study proposes a multi-objective optimization model to obtain the arbitrarily surface textures design of the slipper/swash plate interface for improving the mechanical and volumetric efficiency of the EHA pump. The model is composed of the lubrication film model, the component dynamic model considering the spinning motion, and the multi-objective optimization model. In this way, the arbitrary-shaped surface texture with the best comprehensive effect in the EHA pump is achieved and its positive effects in the EHA pump prototype are verified. Experimental results show a reduction in wear and an improvement in mechanical and volumetric efficiency by 1.4% and 0.8%, respectively, with the textured swash plate compared with the untextured one.

KEYWORDS electro-hydrostatic actuator, axial piston pump, slipper/swash plate interface, multi-objective optimization, surface texture

1 Introduction

The high-speed axial piston pumps are widely used as the main power source in the electro-hydrostatic actuators (EHAs) due to the advantages of compact structure, high power density, and high reliability. The EHA pump has a broad operating range and needs to start up instantly and change shaft rotating direction frequently. Therefore, full fluid film lubrication may be difficult to be established, and severe abrasion of sliding parts will appear, especially in the slipper/swash plate interface. The slipper/swash plate interface is one of the three major tribological contacts of the axial piston pump, and it plays the function of sealing and bearing [1]. Its friction torque and leakage flow determine the mechanical and volumetric efficiencies of the EHA pump [2]. However, the dynamic behaviors of slippers are extremely complex. The external forces such as piston–slipper ball joint friction force and unbalanced centrifugal inertia force generate micro motions between the slipper and the swash plate, such as tilting motion [3], squeezing motion [4], and spinning motion [5]. Thus, the geometry variation in lubricant film

thickness will result in uneven hydrodynamic pressure distribution, and mixed friction areas with severe lubrication conditions will occur [6]. Notably, oxidation and blackening wear traces even appear on the surfaces of components, which greatly affect the efficiency and the lifetime of the EHA pump [7].

The laser surface texturing (LST) technique, which is considered a feasible option for changing the surface topography, can reduce friction and wear of various industrial applications [8]. The enhanced performances are dependent on the abilities of the micro dimples to induce additional hydrodynamic pressure, store lubricants, lower shear gradient, and trap wear debris [9]. Thus, the LST technique is applied to improve the tribological properties of tribosystems. However, the geometric parameters of surface textures are sensitive to the type of contacts and working conditions, and an improperly designed texture pattern will result in detrimental effects on the tribological performance [10].

In the published theoretical studies, most of the studies on surface texture optimization mainly focus on the thrust bearing [11–16] and the mechanical seal [17–19]. However, the minimum gap height between two specimens is constant and does not depend on the oil film

pressure and the external load, while the lubricant film thickness and boundary conditions of the lubricating interfaces in the axial piston pump are time-varying and unevenly distributed, which is profoundly different from thrust bearings and mechanical seals. To overcome this difficulty and apply the optimal LST to the friction pairs in axial piston pumps, many researchers, including the authors' team, have made efforts [8,20–23]. A previous study by the authors' team established the hydrodynamic lubrication model and proposed an optimization model for the multi-scale textured cylinder/valve plate interface [23]. These studies provide the basis for the LST optimization model for the slipper/swash plate interface. However, the following two problems remain to be addressed.

First, the piston–slipper assemblies have multiple degrees of freedom, and their boundary velocities stem from the linear reciprocating and rotating macro-motions and the spinning micro-motions, whose kinematic and hydrodynamic models are different from the cylinder/valve plate interface [24]. Tang et al. [25] and Spencer [26] measured the oil film thickness, pressure, and temperature distributions of the slipper/swash plate interface. However, spinning motion was always ignored or replaced by a constant value while establishing the lubrication model. The experiment results obtained by Zhang et al. [27] confirmed the presence of the spinning motion and showed that the spinning speed approximately varied with shaft speed. Ransegnola et al. [28] introduced a mutual interaction model considering the friction at the ball-socket interface, which also concluded that the spinning speed was highly dependent on the operation conditions. Thus, a spinning motion prediction model is strongly needed to obtain a relatively reliable and accurate velocity boundary of the slipper/swash plate interface in this study.

Some of the effects of the LST on the axial piston pump are contradictory to each other. Murrenhoff et al. [29,30] first applied surface texturing techniques to the friction pairs of the axial piston pump. The results indicate that the surface texture plays the most significant role in improving the carrying capacity of the oil film under the condition of high speed and pressure, which creates a thicker oil film thickness and a higher leakage at the same time. In recent years, the research on surface texture for the slipper/swash plate interface shows that the optimization goals are mainly to analyze the load-carrying capacity of friction pair interfaces [31] and the leakage [32] independently. Therefore, a multi-objective optimization model is needed for the LST to deal with the contradictory effects and comprehensively enhance the performance of the pump.

In this study, an optimization model for the multi-scale textured slipper/swash plate interface in the EHA pump is proposed. A slipper dynamic model is established considering the spinning speed to avoid inaccurate calculation of

the velocity boundary caused by the slipper spinning motion. Instead of focusing on mechanical losses or volumetric losses independently, the oil film load-bearing capacity, viscous friction torque, tilting angle, and leakage are all regarded as optimization objectives. The optimal Pareto solution sets of the surface textured dimple shapes of the slipper/swash plate interface are obtained. The EHA pump prototype equipped with the textured or untextured swash plate is tested on the high-speed pump test rig. The experimental results demonstrate the positive effects of the optimal surface texture on wear reduction and efficiency improvement in EHA pumps.

2 Multi-objective optimization model of the slipper/swash plate interface

2.1 Dynamics

To avoid the long-term mixed friction caused by the serious tilting behavior of the slipper, or the solid contact caused by the difficulty of forming the lubricant film which will finally result in the wear of the component, the dynamics of the piston–slipper assembly is analyzed.

The global coordinate system $O-XYZ$, the additional coordinate system $O_{sw}-X_{sw}Y_{sw}Z_{sw}$, and the additional coordinate system $o_s-x_sy_sz_s$ of the slipper are defined as shown in Fig. 1. The piston–slipper assembly is subjected to F_N , which is generated by the piston chamber pressure F_p , the reciprocating inertia force F_a , and the axial friction force F_f between the cylinder and the piston:

$$F_N = (F_p + F_a + F_f) / \cos \beta_s, \quad (1)$$

$$F_{Ny} = F_N \sin \beta_s, \quad (2)$$

$$F_{Nz} = F_N \cos \beta_s, \quad (3)$$

where β_s is the swash plate angle, and F_{Ny} and F_{Nz} are side forces produced by the swash plate in y - and z -axis, respectively.

The load-bearing capacity F_{oils} of the slipper/swash plate interface needs to be balanced with F_N and the spring-back force F_r which serves to hold the slippers against the retainer. The total torques around the x_s - and the y_s -axis include T_{oilsx} and T_{oilsy} produced by the unevenly distributed pressure fields, T_{tsx} and T_{tsy} caused by viscous friction of oil film, friction torque caused by friction force F_{fps} of the spherical joint, and torque produced by centrifugal force F_{cs} acting on the centroid of slippers. The viscous friction of the oil film on the slipper land also produces the torque T_{tsz} , which affects the spinning motion of the slipper as well:

$$T_{tsz} + T_{fps} = I_{zs} \frac{d\omega_{zs}}{dt}, \quad (4)$$

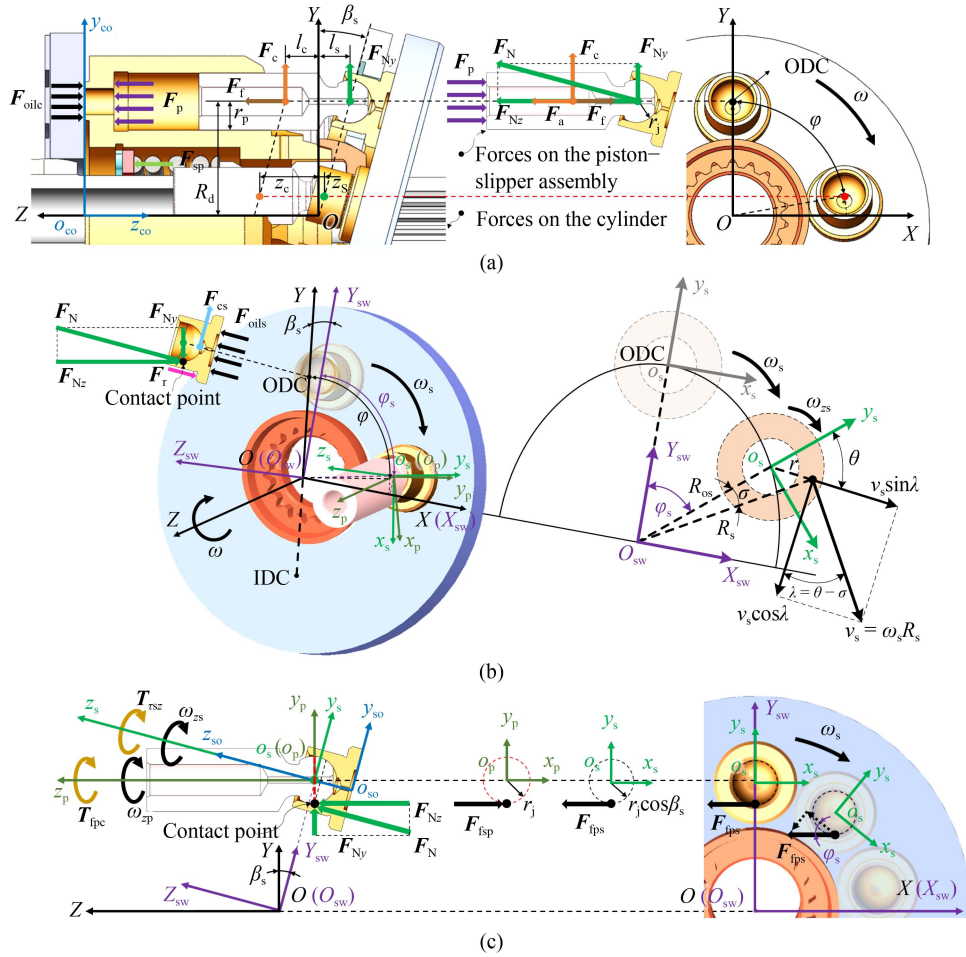


Fig. 1 Axial piston pump kinematics: (a) cylinder and piston–slipper assembly, (b) slipper, and (c) spinning motion of piston and slipper. ODC: outer dead center, IDC: inner dead center.

$$T_{fps} = F_{fps} \cdot (r_j \cos \beta_s), \quad (5)$$

where I_{zs} is the inertia moment of the slipper about the z_s -axis, ω_{zs} is the spinning speed of the slipper, t is time, T_{fps} is the friction torque of the slipper caused by the spherical joint, and r_j is the radius of the spherical joint.

The force and moment equilibrium equations of slippers are given in Eq. (6):

$$\begin{cases} F_{oils} + F_N + F_r = 0, \\ T_{oilsx} + T_{tsx} + F_{fps} \sin \varphi_s (r_j \sin \beta_s) + F_{cs} l_{cs} = 0, \\ T_{oilsy} + T_{tsy} + F_{fps} \cos \varphi_s (r_j \sin \beta_s) = 0, \end{cases} \quad (6)$$

with

$$F_r = F_{sp} / (n_p \cdot \cos \beta_s), \quad (7)$$

where φ_s is the rotation angle of o_s in the $O_{sw}-X_{sw}Y_{sw}Z_{sw}$ system, l_{cs} is the length between the center of the spherical joint and the centroid of the slipper, F_{sp} is spring force in the cylinder center, and n_p is the number of the piston.

2.2 Pressure governing equations

The fluid domain of the lubricant film of the slipper/

swash plate interface is ring-shaped. As shown in Fig. 2, the coordinate system $o_{so}-x_{so}y_{so}z_{so}$ is defined for the fluid domain, and it is obtained by translating the $o_s-x_sy_z$ system from the origin o_s to the origin o_{so} . In the fine-meshed region determined by the radial coordinate R_{ds} and R_{de} , and the azimuth coordinate θ_{ds} and θ_{de} , four identical micro-dimples are formed, which are arranged in two rows along the radial direction and two columns along the circumferential direction. As shown in Fig. 3, the optimization model uses four dimples rather than a single one to consider interactions between adjacent dimples. The parameters of arbitrary shapes are a set of radial coordinates R_{op} , which are distributed at equal angular intervals in the direction of 0° – 360° . As shown in Fig. 3 [23], too many decision variables R_{op} will result in a spiny divergent shape which is difficult to process in the application. Therefore, the number of R_{op} is set as 12 [23] in this model.

The gap height h of any point $P(r, \theta)$ on the slipper/swash plate interface can be derived from the functions h_1 , h_2 , and h_3 , which are the heights of points A , B , and C determined by the time-dependent external load,

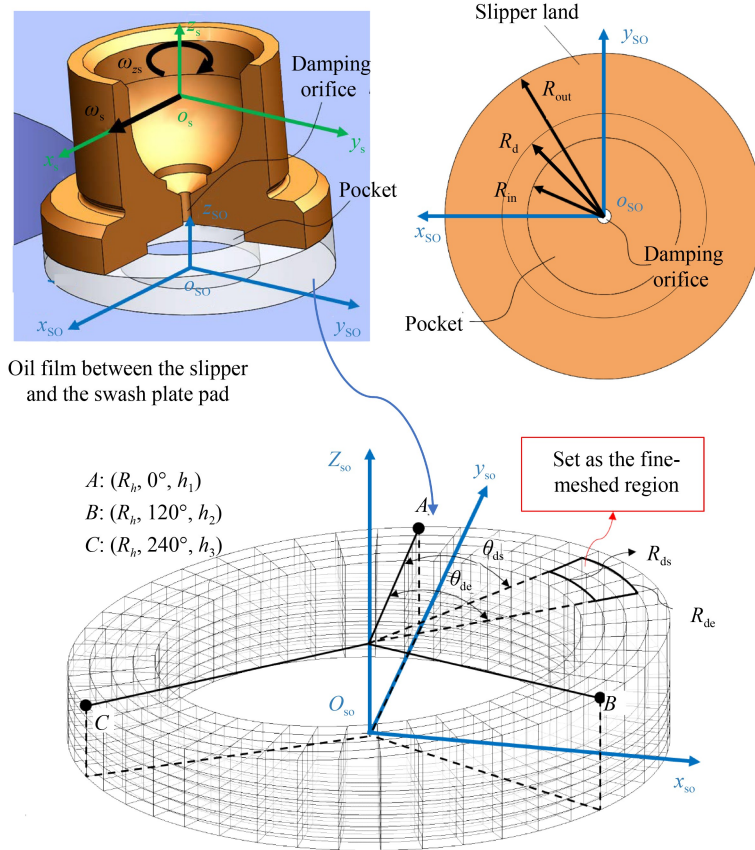


Fig. 2 Oil film domain of the slipper/swash plate interface.

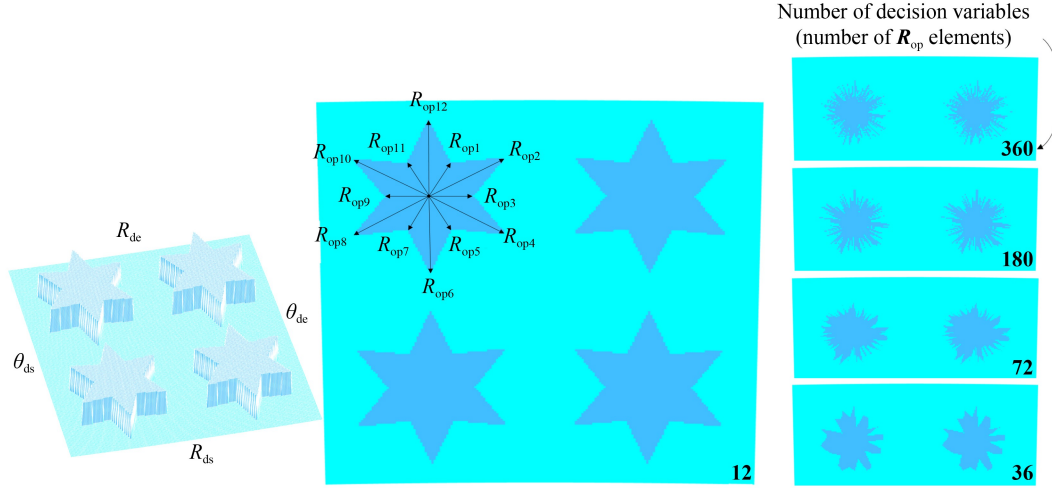


Fig. 3 Arbitrary dimple shapes characterized by R_{op} and four identical micro-dimples [23].

as shown in Eq. (8):

$$h = \frac{1}{\sqrt{3}R_h}(h_2 - h_3)r \sin \theta + \frac{1}{3R_h}(2h_1 - h_2 - h_3)r \cos \theta + \frac{1}{3}(h_1 + h_2 + h_3), \quad (8)$$

where R_h is the oil film radius, and h_1 , h_2 , and h_3 are the gap heights of points A , B , and C , respectively.

The macro-motion of the slipper forms an elliptical trajectory on the $X_{sw}-Y_{sw}$ plane. The relationship between the origin o_s and the shaft rotation angle φ in the coordinate system $O_{sw}-X_{sw}Y_{sw}Z_{sw}$ is given as Eq. (9):

$$\begin{cases} R_{os} = R_d \sqrt{1 + \tan^2 \beta_s \cos^2 \varphi}, \\ \varphi_s = \arctan(\cos \beta_s \tan \varphi), \end{cases} \quad (9)$$

with

$$\varphi = \omega t, \quad (10)$$

where R_{os} is the length between o_s and the Z_{sw} -axis, R_d is the distribution radius of slippers, and ω is rotation speed.

Considering the spinning speed ω_{zs} of the slipper, the radial and circumferential velocities of any point $P(r, \theta)$ can be expressed as Eq. (11). A more detailed explanation of the slipper spinning motion is included in Chao et al. [1]:

$$\begin{cases} v_r = \omega_s R_s \sin(\theta - \sigma), \\ v_\theta = \omega_s R_s \cos(\theta - \sigma) + \omega_{zs} r, \end{cases} \quad (11)$$

with

$$\omega_s = \frac{d\varphi_s}{dt}, \quad (12)$$

$$R_s = \sqrt{R_{os}^2 + r^2 + 2R_{os}r \cos \theta}, \quad (13)$$

$$\sigma = \arcsin(r \sin \theta / R_s), \quad (14)$$

where v_r and v_θ are radial and circumferential velocities at any position (r, θ) of the slipper bottom, respectively, ω_s is the speed of o_s about the Z_{sw} , R_s is the length between point $P(r, \theta)$ and the Z_{sw} -axis, and σ is the angle between $P-O_{sw}$ and o_s-O_{sw} .

The leakage flow rate of the slipper/swash plate interface is given by Eq. (15):

$$Q_{ss} = \int_0^{2\pi} \int_0^h (v_{or} r) \Big|_{r \in [R_{in}, R_{out}]} dz d\theta, \quad (15)$$

with

$$v_{or} = \frac{1}{2\eta} \frac{\partial p}{\partial r} (z^2 - hz) + v_r \frac{z}{h}, \quad (16)$$

where Q_{ss} is leakage, v_{or} is the radial velocity of the oil, R_{in} and R_{out} are the inner and outer radii of the slipper land, respectively, η is the oil dynamic viscosity, and p is the oil film pressure.

The oil film between the slipper/swash plate interface is assumed to be incompressible and laminar. At the same time, the velocity of the fluid attached to the wall is considered same as that of the wall without considering the wall slip phenomenon [14,33]. The Reynolds equation [34] in polar coordinates is derived as shown in Eq. (17):

$$\begin{aligned} & \frac{1}{\eta r} \frac{\partial}{\partial r} \left(r h^3 \frac{\partial p}{\partial r} \right) + \frac{1}{\eta r^2} \frac{\partial}{\partial \theta} \left(h^3 \frac{\partial p}{\partial \theta} \right) \\ &= \frac{1}{r} \frac{\partial}{\partial r} (rv_r h) + 6 \frac{1}{r} \frac{\partial}{\partial \theta} (v_\theta h) + 12 \frac{\partial h}{\partial t} + \frac{3\rho}{10\eta r} \frac{\partial}{\partial r} (v_\theta^2 h^3), \end{aligned} \quad (17)$$

where ρ is oil density.

The load-bearing capacity F_{oils} , viscous friction torque about the z_s -axis T_{tsz} , and viscous friction torque about the Z_{sw} -axis T_{tszg} can be solved by the Reynolds equation with the pressure and velocity boundary conditions:

$$F_{oils} = \int_0^{2\pi} \int_{R_{in}}^{R_{out}} pr dr d\theta, \quad (18)$$

$$T_{tsz} = \int_0^{2\pi} \int_{R_{in}}^{R_{out}} \tau_{o\theta}|_{z=h} \cdot r^2 dr d\theta, \quad (19)$$

$$T_{tszg} = \int_0^{2\pi} \int_{R_{in}}^{R_{out}} [\tau_{o\theta}|_{z=h} \cdot \cos(\theta - \sigma) + \tau_{or}|_{z=h} \cdot \sin(\theta - \sigma)] \cdot R_s r dr d\theta, \quad (20)$$

with

$$\tau_{o\theta}|_{z=h} = \frac{h}{2r} \frac{\partial p}{\partial \theta} + \eta \frac{v_\theta}{h}, \quad (21)$$

$$\tau_{or}|_{z=h} = \frac{h}{2} \frac{\partial p}{\partial r} + \eta \frac{v_r}{h} - \frac{\rho h}{4r} v_\theta^2, \quad (22)$$

where $\tau_{o\theta}$ and τ_{or} are circumferential and radial viscous shear stresses, respectively.

In the simulation model, the main dimensions, working conditions, and oil parameters of the EHA pump are listed in Table 1.

2.3 Simulation model

The flowchart of the multi-objective optimization model of the slipper/swash plate interface is shown in Fig. 4. The model is mainly composed of three parts: the oil film characteristic module, the force and torque balance module, and the multi-objective optimization module based on the non-dominated sorting genetic algorithm II (NSGA-II), which is confirmed to be an effective method to solve the multi-objective optimization problem [23].

Simultaneously, the model needs to consider not only the tilting motion but also the spinning motion of the piston and the slipper. Thus, the oil film characteristic module needs to be executed constantly to obtain pocket pressure p_{ops} which is regarded as one of the current pressure boundary conditions to satisfy the flow continuity equation. Then, p_{ops} is constantly called by the force and torque balance module. Finally, when the slipper reaches the force and torque balance, the spinning motion driving or hindering torque can be substituted into

Table 1 EHA pump parameters and operating conditions considered in this study

Parameter	Value
Distribution radius of slippers, R_d	0.02 m
Piston radius, r_p	0.005 m
Inlet pressure, p_{in}	5×10^5 Pa
Outlet pressure, p_{out}	28×10^6 Pa
Case drain pressure, p_0	1×10^5 Pa
Atmospheric saturation pressure	3×10^4 Pa
Shaft speed, n	10000 r/min
Swash plate angle, β_s	0.13 rad (7.5°)
Temperature	60 °C
Oil density at 60 °C	837.4 kg/m³
Oil kinematic viscosity at 60 °C	10.3 mm²/s

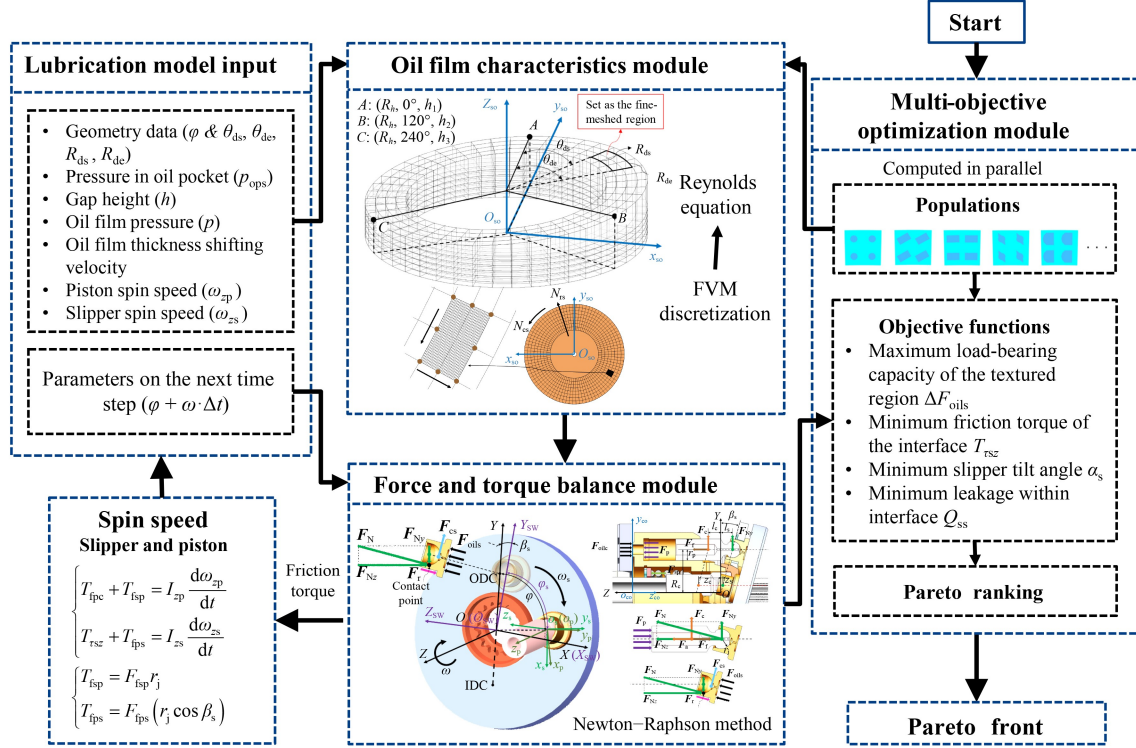


Fig. 4 Flowchart of the multi-objective optimizing procedure for the slipper/swashplate interface. IDC: inner dead center, ODC: outer dead center.

the spinning motion module. The module also solves the spinning angular acceleration at the current moment t and the spinning velocity at the next moment ($t + \Delta t$) to obtain new velocity boundary conditions. Regarding one entire shaft revolution as a cycle, the model needs to be executed for at least eight cycles under any working conditions to acquire periodic variation of lubricant film characteristics and micro-motion characteristics of rotating components.

During the simulation process, if the surface textures produced by each individual in a population are all evaluated for eight cycles, then the simulation time will be prolonged thousands of times. Thus, the multi-objective optimization module is set to start the additional fine-meshed region optimization where the slipper is most likely to produce wear due to the excessive tilting angle. The changing surface topography only varies the load capacity of the textured fine-meshed region but not the entire slipper/swash plate interface. As a result, the difference between local load-bearing capacity at the textured fine-meshed region $F_{\text{oils}\{\text{textured}\}}$ and untextured region $F_{\text{oils}\{\text{untextured}\}}$, namely ΔF_{oils} , is selected as a surrogate objective of F_{oils} as shown in Eq. (23):

$$\Delta F_{\text{oils}} = F_{\text{oils}\{\text{textured}\}} - F_{\text{oils}\{\text{untextured}\}}. \quad (23)$$

According to Eqs. (18) and (19), the mechanical efficiency η_m is expressed as Eq. (24) under the simulation condition:

$$\eta_m = \frac{(p_{\text{out}} - p_{\text{in}}) V_s}{2\pi [T_{ss} + (T_{tsz} + 0.2)\cos\beta_s \sqrt{1 - \cos^2\varphi \sin^2\beta_s}]}, \quad (24)$$

where V_s is the displacement of the pump, and T_{ss} is the output torque of the shaft in addition to viscous friction torque of the slipper/swash plate interface. η_m increases with the decrease in T_{tsz} . As a result, T_{tsz} can be considered the optimization objective.

Based on the authors' previous attempts at different depths during the study, the recommended value of dimple depth in this simulation is 5 μm . Under the fixed dimple depth condition, the objective of the simulation model is to find the optimal radial coordinate array R_{op} of the dimple shape. This way maximizes the load-bearing capacity ΔF_{oils} and minimizes the tilting angle α_s , the viscous friction torque T_{tsz} , and the leakage Q_{ss} of the slipper/swash plate interface.

The NSGA-II parameters utilized in the multi-objective optimization model are listed in Table 2.

3 Simulation results and discussion

The simulated slipper tilting angle α_s and the tilting azimuth angle of the untextured slipper/swash plate interface θ_{as} are shown in Fig. 5. In the last three revolutions, the range of the maximum tilting angle varies from 0.00564° to 0.00578°, which is located at the azimuth angle of 175.5°–179.1° and the shaft rotation

angle of $308^\circ\text{--}314^\circ$. The slipper tends to form the maximum tilting angle on the low-pressure side near the outer dead center (ODC). Based on the simulation data, the additional fine-meshed region where the slipper has a maximum tilting angle is then located. The specific parameters are listed in [Table 3](#).

The rank of individuals is realized by comparing it with the objective function at the next shaft rotation angle ($\varphi_{op} + \omega\Delta t$). The Pareto non-dominated solution set can be obtained after the algorithm searches exceed the stall generations and the average change in the spread reaches the pre-set tolerance. After the multi-objective optimization model reaches the termination condition, the Pareto optimal solution set is generated. The dimple shapes represented by the optimal solution are shown in [Fig. 6](#).

Table 2 Parameters of multi-objective optimization model based on NSGA-II

Parameter	Value
Dimple depth	$5 \mu\text{m}$
Number of R_{op} elements	12
Population size	60
Pareto fraction	0.35
Crossover fraction	0.8
Migration fraction	0.2
Lower bounds	$\geq 0.1 \text{ mm}$
Upper bounds	$\leq 0.2 \text{ mm}$
Objectives	1. Maximization ΔF_{oils} 2. Minimization T_{rsz} 3. Minimization α_s 4. Minimization Q_{ss}

The Pareto front of the slipper/swash plate interface is depicted in [Fig. 7](#). The dimple shapes of the 9th and 10th results are similar to the arc-sided square, which produce the maximum lubricant film capacity of load carrying and minimum tilting angle. Meanwhile, the dimple shapes of the 5th and 21st results are approximated as water-drop shapes, which minimize the leakage flow. The dimple shape of the 1st result is circular, which decreases the viscous friction torque. The dimple shape parameters R_{op} which conclude the representative optimization results are listed in [Table 4](#). When the radial size accuracy is only 1 μm , the dimple shapes between the 9th and 10th results and the 5th and 21st results are considered identical. In addition, the overall approximate water-drop-shaped dimple is nearly similar to a circle because of its small sharp angle.

The pressure and gap height distributions produced by the optimal dimple shapes of the slipper/swash plate interface are shown in [Fig. 8](#). The dynamic pressure caused by different dimple shapes has obvious differences. The pressure distribution curves along the cylinder rotation direction produced by the approximate water-drop-shaped dimples (No. 5) and the approximate arc-sided square-shaped dimple (No. 9) are shown in [Fig. 9](#). The positions where the maximum dynamic pressures are generated and the positions at which the atmospheric saturation pressures are reached are different. The maximum dynamic pressure produced by the approximate arc-sided square-shaped dimple (No. 9) is about 5 MPa higher than that produced by the approximate water-drop-shaped dimples (No. 5). This condition allows the approximate arc-sided square-shaped dimple (No. 9) to generate maximum load-bearing capacity.

The load-bearing capacity of the untextured region is

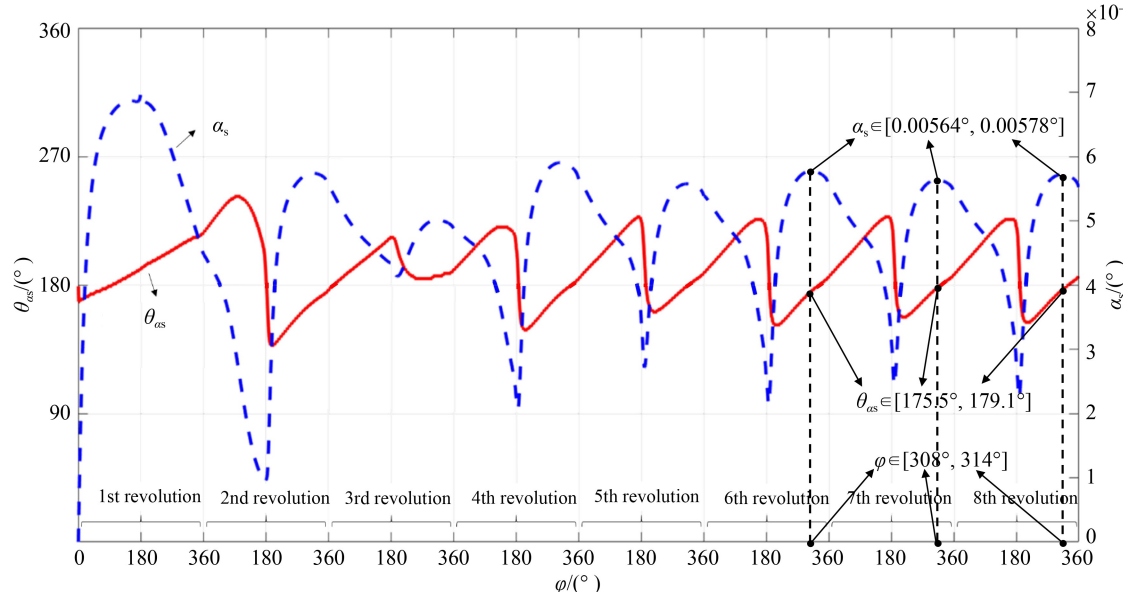


Fig. 5 Periodic changes of the slipper tilting angle and the tilting azimuth angle.

1.653 N. The rate of changes in four optimizing targets (r_{perf}) is calculated as

Table 3 Fine-meshed region positional parameter and starting shaft rotation angle φ_{op}

Parameter	Value
θ_{ds}	3 rad (171.90°)
θ_{de}	3.19 rad (182.70°)
R_{ds}	5×10^{-3} m
R_{de}	6.05×10^{-3} m
φ_{op}	36.83 rad (2110°)

$$r_{\text{perf}} = (V_{\text{textured}} - V_{\text{untextured}})/V_{\text{untextured}}, \quad (25)$$

where V is replaced by F_{oils} , α_s , T_{rsz} , and Q_{ss} when evaluating the load bearing capacity, tilt angle, friction torque, and leakage, respectively.

As shown in Fig. 10, the surface texture plays a positive role in improving the capacity of load carrying, but it weakly reduces the viscous friction torque, tilting angle, and leakage. Although approximate arc-sided square-shaped dimple (No. 9) has little effect on reducing viscous friction torque and leakage, it increases the load-bearing capacity of the slipper/swash plate interface by

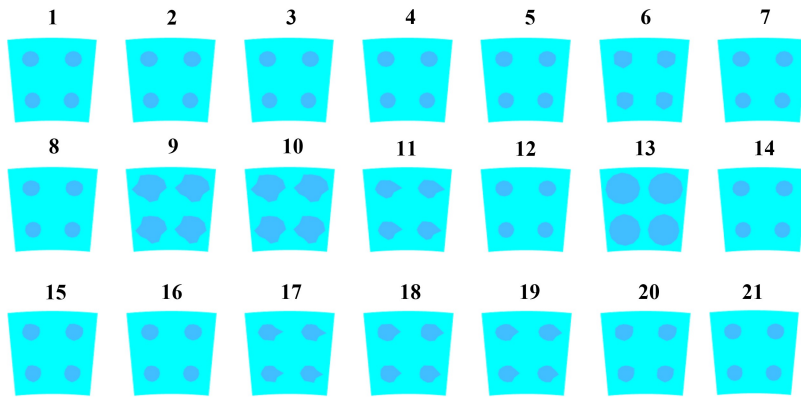


Fig. 6 Dimple shape represented by the optimal solution on the Pareto front.

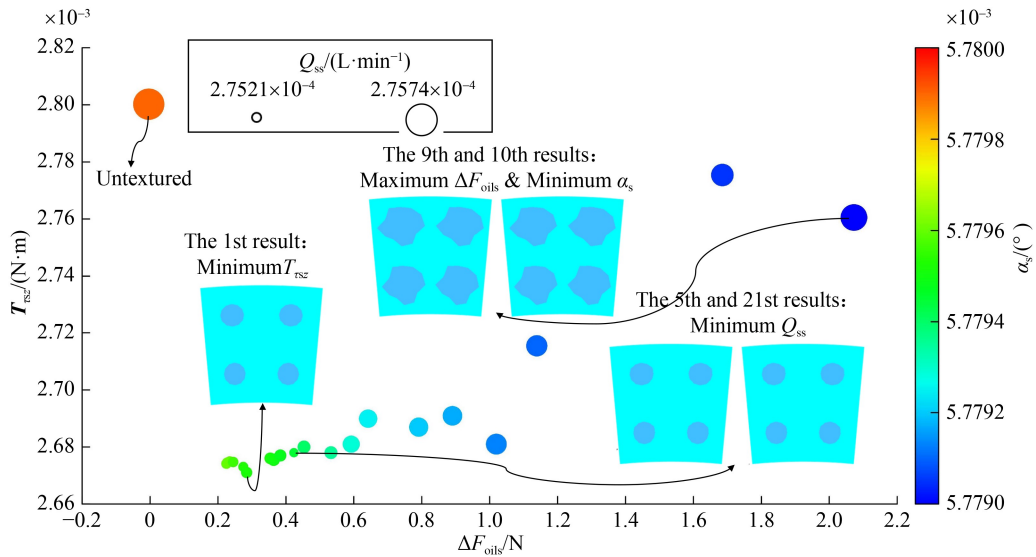


Fig. 7 Pareto front with the optimal results.

Table 4 Optimal R_{op} with corresponding dimple shapes

Dimple shape	R_{op} /mm	Shape
1	[0.100, 0.100, 0.100, 0.100, 0.100, 0.100, 0.100, 0.100, 0.100, 0.100, 0.100]	Circle
5	[0.100, 0.108, 0.100, 0.100, 0.100, 0.100, 0.100, 0.100, 0.103, 0.100, 0.100]	Similar to water drop
9	[0.185, 0.200, 0.200, 0.142, 0.179, 0.175, 0.130, 0.156, 0.200, 0.148, 0.193, 0.173]	Approximate arc-sided square
10	[0.185, 0.200, 0.200, 0.142, 0.179, 0.175, 0.130, 0.156, 0.200, 0.148, 0.193, 0.173]	Approximate arc-sided square
21	[0.100, 0.108, 0.100, 0.100, 0.100, 0.100, 0.100, 0.100, 0.103, 0.100, 0.100]	Similar to water drop

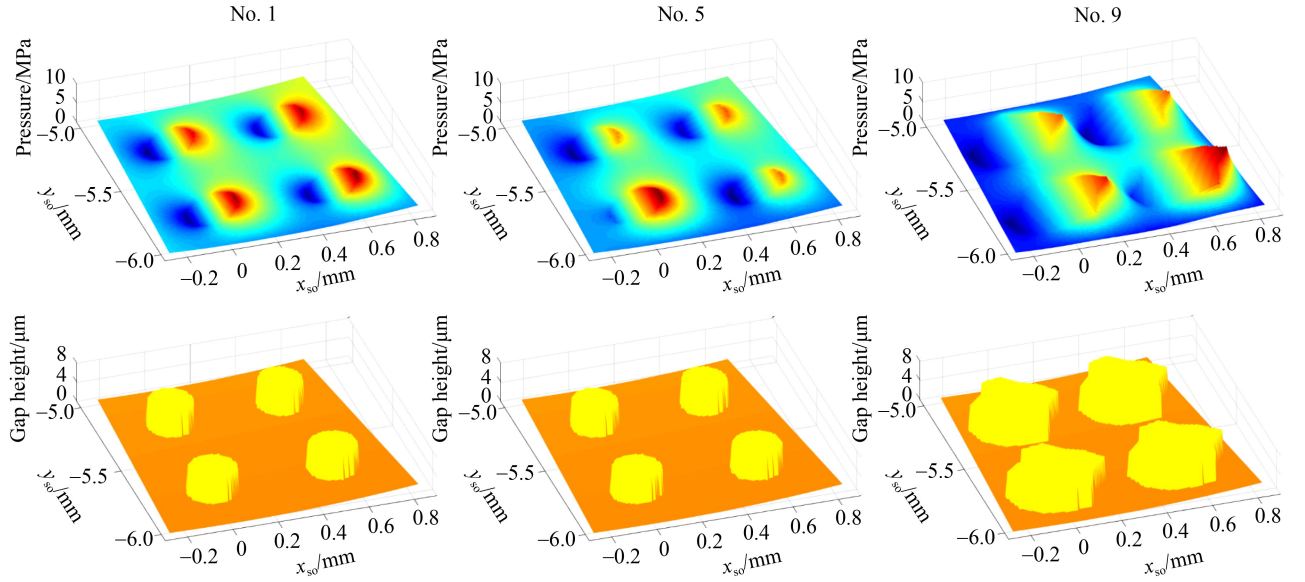


Fig. 8 Pressure distribution and gap height distribution of the textured region with Nos. 1, 5, and 9 dimple shapes.

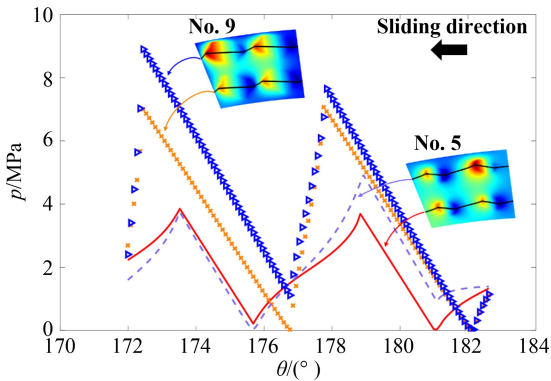


Fig. 9 Pressure distribution curves along the circumferential direction of the slipper land with Nos. 5 and 9 dimple shapes.

123.77% compared with the untextured one, whose optimization effect is significantly greater than that of approximate water-drop-shaped dimple (No. 5).

4 Experiment verification

4.1 Experimental scheme

The real effects of the surface texture scheme in the EHA pump are evaluated on a test rig that is used in the previous work, as shown in Fig. 11, to verify the optimal solution of arbitrary-shaped surface textures for the slipper/swash plate interface discussed in Section 3. The test rig can provide a rotational speed of up to 16000 r/min and can measure variables such as inlet, outlet, and leakage pressure, outlet and leakage flow, shaft speed, and shaft torque.

According to the simulation results of optimal dimple

shapes in Section 3, the approximate arc-sided square-shaped dimple (No. 9) generates the maximum load-bearing capacity and the minimum tilting angle. Therefore, the wear marks of the approximate arc-sided square-shaped (No. 9) textured swash plate are compared with those of the untextured one. The texture pattern is fabricated on the swash plate using a Q-switched Nd:YVO₄ laser machine with a wavelength of 355 nm, a frequency of 30 kHz, and a maximum output power of 5 W [35]. Slippers are prone to tilt toward the splined shaft. Thus, the surface texture is arranged in the negative y_{so} -axis region and the total number of dimples is 1224 (radial 3 rows \times circumferential 192 rows + radial 3 rows \times circumferential 216 rows). By transforming the slipper bottom coordinate from the $o_s-x_s-y_s-z_s$ coordinate system to the $O_{sw}-X_{sw}Y_{sw}Z_{sw}$ coordinate system, the surface topography parameters of the static swash plate surface can be converted to the slipper land surface which is revolving around. The textured swash plate and dimples on the surface are shown in Fig. 12.

The tested components and their abbreviations are the textured swash plate (TSP) and the untextured swash plate (UTSP). Before the test, the components are cleaned in an ultrasonic acetone bath to remove the contaminants. The assembly of the swash plate with the texture design is shown in Fig. 13. After the test, the macroscopic views of the swash plate are observed by a confocal laser scanning microscope (CLSM).

For better observations of the surface wear marks of the components, a relatively severe operating condition is chosen. When the EHA pump pressure reaches 28 MPa, the tilting angle of the swash plate will be reduced to 1.2°, and the pump only needs to run for a very short time. Thus, the prototype is operated for 20 min at the maximum rotational speed of 10000 r/min and maximum pressure condition of 28 MPa. The tested EHA pump

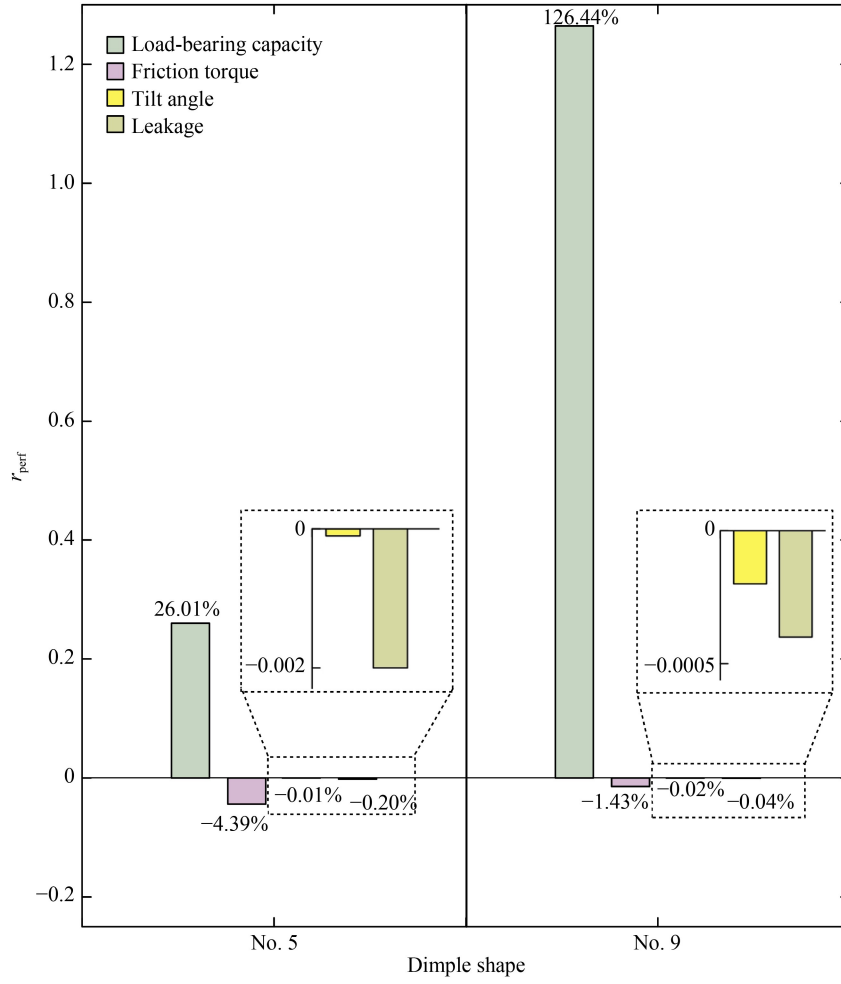


Fig. 10 Rate of changes in four optimizing targets with the optimal results.

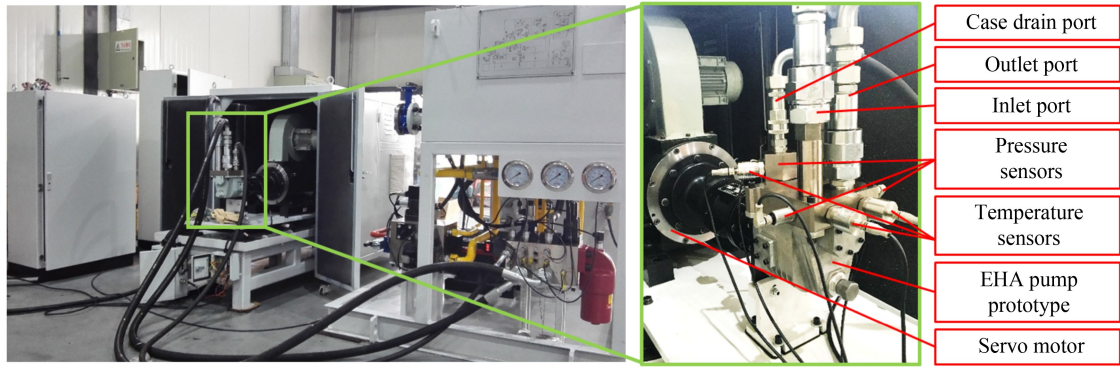


Fig. 11 Test rig used for evaluating the performance of EHA pumps. EHA: electro-hydrostatic actuator.

prototype will be equipped with TSP or UTSP.

4.2 Wear of the swash plate surface

The macroscopic views of the UTSP and TSP interface are shown in Fig. 14. The black boxes correspond to the position where the slider causes the largest tilting angle. Compared with the wear marks in the black box of UTSP,

the wear marks of TSP at the same place are not obvious. The characteristics discussed above can be confirmed by the CLSM scanned image of the UTSP and the TSP as shown in Fig. 15. Deep plowing marks of 1–2 μm generated by wear debris can be found on the UTSP surface, which are more obvious than that of the TSP. This phenomenon indicates that the sliders sliding against the UTSP have a greater degree of tilting

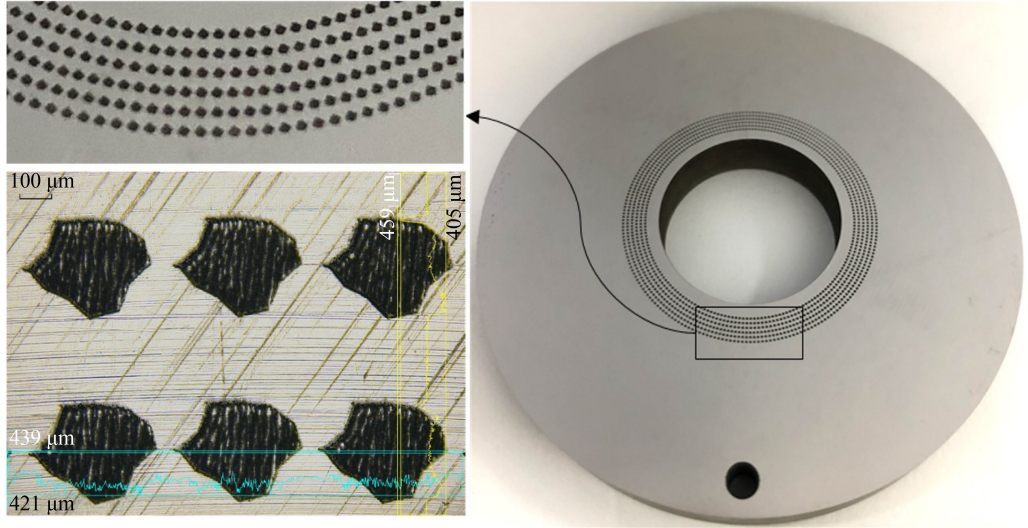


Fig. 12 Textured swash plate and dimples on the surface.



Fig. 13 Assembly of the swash plate with texture design.

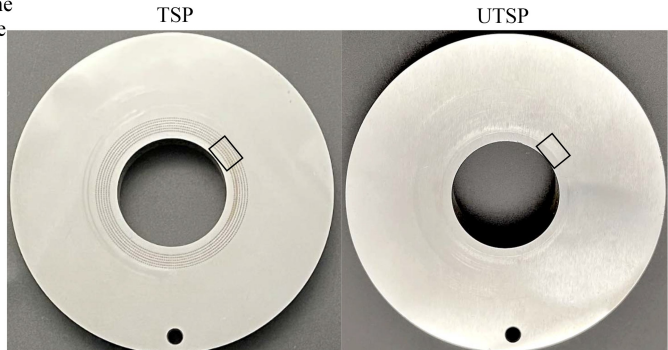
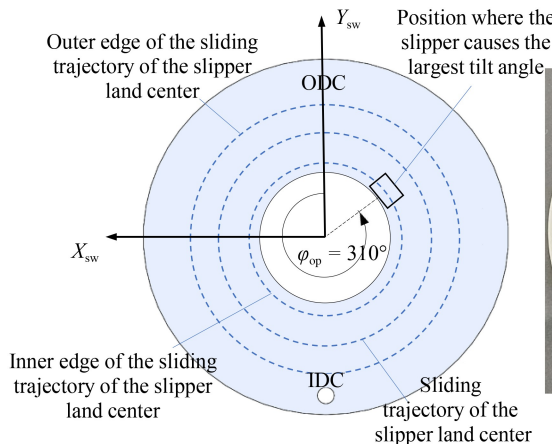


Fig. 14 Photos of the tested TSP and UTSP marked with rectangular frames. IDC: inner dead center, TSP: textured swash plate, UTSP: untextured swash plate, ODC: outer dead center.

behavior, which results in serious abrasive wear. By contrast, the surface texture of the TSP weakens the tilting behavior of the slipper and enhances the load-bearing capacity at the position where the slipper causes the largest tilting angle. The ability of the dimples to trap wear debris is also proven.

4.3 Efficiencies of EHA pump prototype

The performance data of the EHA pump prototype equipped with TSP and UTSP are shown in Table 5. The mechanical efficiency η_m and volumetric efficiency η_v are calculated according to Eqs. (26) and (27), respectively:

$$\eta_m = \frac{(p_{\text{out}} - p_{\text{in}}) V_g}{2\pi T_{\text{sh}}} \times 100\%, \quad (26)$$

$$\eta_v = \frac{q_{\text{out}}}{V_g n} \times 100\%, \quad (27)$$

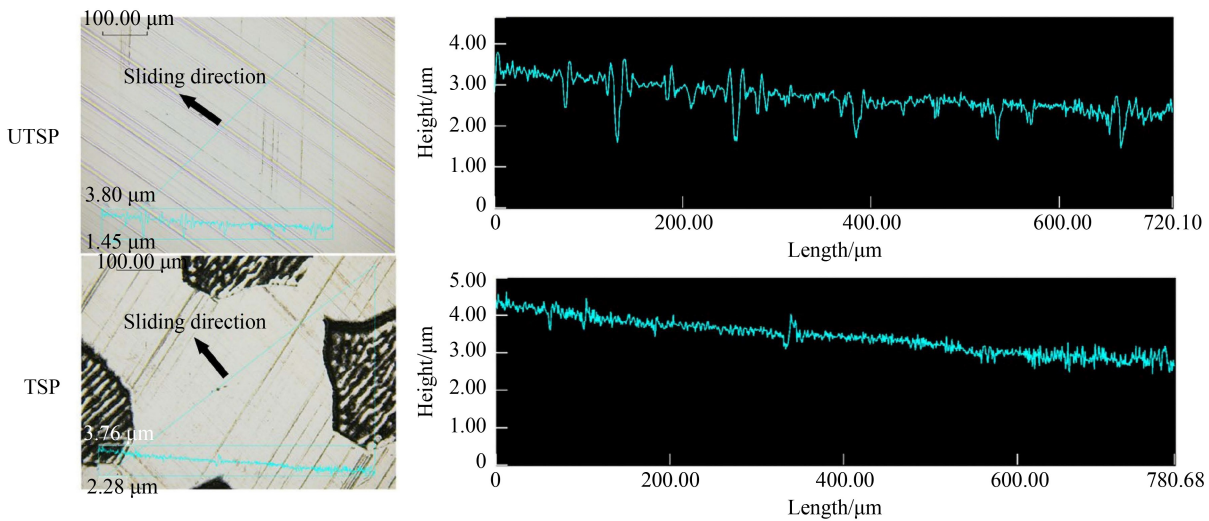


Fig. 15 CLSM scanned images of the TSP and the UTSP after testing at the position where the slipper causes the largest tilting angle. TSP: textured swash plate, UTSP: untextured swash plate, CLSM: confocal laser scanning microscope.

Table 5 Efficiencies and output torques of EHA prototype at 10000 r/min, 28 MPa

EHA pump prototype equipped with	Mechanical efficiency, $\eta_{\text{m}}/\%$	Volumetric efficiency, $\eta_{\text{v}}/\%$	Output torque, $T_{\text{sh}}/(\text{N}\cdot\text{m})$
TSP	87.1	81.1	18.6
UTSP	85.7	80.3	18.9

where q_{out} is the outlet flow and T_{sh} is the output torque of the shaft of the prototype.

Table 5 shows that the TSP improves the mechanical efficiency by 1.4%. The direct reason for the improvement of mechanical efficiency is that the TSP reduces the T_{sh} of the prototype by 0.3 N·m. However, the improvement effect of the TSP on the volumetric efficiency of the EHA pump prototype is not obvious, and it is less than 1%.

5 Conclusions

From all the simulation and experiment results performed, the following conclusions can be drawn:

A multi-objective optimization model for the multi-scale textured slipper/swash plate interface based on the NSGA-II is proposed. The optimal Pareto solution sets of the surface textured dimple shapes are obtained. In the simulation, the approximate arc-sided square-shaped dimple (No. 9) reduces the friction torque, tilting angle, and leakage, and it increases the load-bearing capacity of the slipper/swash plate interface by 123.77%. In the experiment, the No. 9 dimple improves the mechanical and volumetric efficiencies of the EHA pump prototype by 1.4% and 0.8%, respectively.

The effects of thermoelastic deformation of the solid parts will be considered in the future work to refine the model. The three modules of the optimization model are also required to further improve the computational efficiency and shorten the simulation time.

Nomenclature

Abbreviations

CLSM	Confocal laser scanning microscope
EHA	Electro-hydrostatic actuator
LST	Laser surface texturing
IDC	Inner dead center
ODC	Outer dead center
TSP	Textured swash plate
UTSP	Untextured swash plate

Variables

F_a	Reciprocating inertia force
F_{cs}	Slipper centrifugal force
F_f	Axial friction force between the cylinder and the piston
F_{fps}	Friction force of the slipper caused by the spherical joint
F_N	Normal force produced by the swash plate of the piston–slipper assembly
F_{Ny}, F_{Nz}	Side force produced by the swash plate in y - and z -axis, respectively
F_{oils}	Load-bearing capacity force of the slipper/swash plate interface
$F_{\text{oils}\{\text{textured}\}}$	Local load-bearing capacity at the textured fine-meshed and untextured regions, respectively
$F_{\text{oils}\{\text{untextured}\}}$	

F_p	Piston chamber pressure	η_v	Volumetric efficiency
F_r	Spring-back force	θ	Azimuth angle
F_{sp}	Spring force in the cylinder center	θ_{as}	Tilting azimuth angle of the slipper
ΔF_{oils}	Difference of local load-bearing capacity at textured region and untextured region	θ_{ds}, θ_{de}	Azimuth coordinate of the fine-meshed region
h	Gap height	ρ	Oil density
I_{zs}	Inertia moment of the slipper about the z_s -axis	σ	Angle between any position $(r, \theta) - O_{sw}$ and $o_s - O_{sw}$
l_{cs}	Length between the center of the spherical joint and the centroid of the slipper	φ_{op}	Shaft rotation angle
n	Shaft speed	φ_s	Starting shaft rotation angle of the optimization process
n_p	Number of the piston	ω_s	Rotation angle of o_s in the $O_{sw}-X_{sw}Y_{sw}Z_{sw}$ system
p	Oil film pressure	ω	Rotation speed
p_0	Case drain pressure	ω_s	Rotation speed of o_s about the Z_{sw} -axis
p_{in}, p_{out}	Inlet and outlet pressures, respectively	ω_{zs}	Spinning speed of the slipper
p_{ops}	Pocket pressure	$\tau_{0\theta}, \tau_{or}$	Circumferential and radial viscous shear stresses, respectively
q_{out}	Outlet flow		
Q_{ss}	Leakage		
r	Radius		
r_j	Radius of the spherical joint		
r_p	Piston radius		
r_{perf}	Rate of changes in four optimizing targets, i.e., $F_{oils}, \alpha_s, T_{rsz}$, and Q_{ss}		
R_d	Distribution radius of slippers		
R_{ds}, R_{de}	Radial coordinate of the fine-meshed region		
R_h	Oil film radius		
R_{in}, R_{out}	Inner and outer radii of the slipper land, respectively		
R_{os}	Length between o_s and the Z_{sw} -axis		
R_s	Length between any position (r, θ) and the Z_{sw} -axis		
R_{op}	Array of the radial coordinates defining the arbitrary dimple shape		
t	Time		
T_{fps}	Friction torque of the slipper caused by the spherical joint		
T_{oilxr}, T_{oilzy}	Torques produced by the unevenly distributed pressure fields of the oil film about the x_s - and y_s -axis, respectively		
T_{sh}	Output torque of the shaft of the prototype		
T_{ss}	Output torque of the shaft in addition to viscous friction torque of the slipper/swash plate interface		
$T_{rsx}, T_{rsy},$	Viscous friction torques about the x_s -, y_s -, z_s -, and Z_{sw} -axis, respectively		
T_{rsz}, T_{rszg}			
v_{or}	Radial velocity of the oil		
v_r, v_θ	Radial and circumferential velocities at any position (r, θ) of the slipper bottom, respectively		
V_s	Displacement of the pump		
α_s	Tilting angle of the slipper		
β_s	Swash plate angle		
η	Oil dynamic viscosity		
η_m	Mechanical efficiency		

Acknowledgements The research was financially supported by the National Key R&D Program of China (Grant No. 2018YFB2001101), the National Outstanding Youth Science Foundation of China (Grant No. 51922093), the National Science Foundation for Young Scientists of China (Grant No. 51905473), the Major Science and Technology Projects in Ningbo, China (Grant No. 2019B10054), and the Open Foundation of the State Key Laboratory of Mechanical Transmissions, China (Grant No. SKLMT-ZDKFKT-202001).

References

- Chao Q, Zhang J H, Xu B, Wang Q N. Discussion on the Reynolds equation for the slipper bearing modeling in axial piston pumps. *Tribology International*, 2018, 118: 140–147
- Bergada J M, Watton J, Haynes J M, Davies D L. The hydrostatic/hydrodynamic behaviour of an axial piston pump slipper with multiple lands. *Meccanica*, 2010, 45(4): 585–602
- Manring N D, Mehta V S, Nelson B E, Graf K J, Kuehn J L. Scaling the speed limitations for axial-piston swash-plate type hydrostatic machines. *Journal of Dynamic Systems, Measurement, and Control*, 2014, 136(3): 031004
- Xu B, Zhang J H, Yang H Y. Investigation on structural optimization of anti-overturning slipper of axial piston pump. *Science China Technological Sciences*, 2012, 55(11): 3010–3018
- Hooke C J. The effects of centrifugal load and ball friction on the lubrication of slippers in axial piston pumps. In: Proceedings of the 6th International Fluid Power Symposium. Cambridge: BHRA Fluid Engineering, 1981, 179–191
- Ernst M, Vacca A. Hydrostatic vs. hydrodynamic components of fluid pressure in the tribological interfaces of axial piston machines. *Tribology International*, 2021, 157: 106878
- Chao Q, Zhang J H, Xu B, Wang Q N, Lyu F, Li K. Integrated slipper retainer mechanism to eliminate slipper wear in high-speed axial piston pumps. *Frontiers of Mechanical Engineering*, 2022, 17(1): 1–13
- Shin J H, Kim K W. Effect of surface non-flatness on the lubrication characteristics in the valve part of a swash-plate type

- axial piston pump. *Meccanica*, 2014, 49(5): 1275–1295
9. Etsion I. State of the art in laser surface texturing. *Journal of Tribology*, 2005, 127(1): 248–253
 10. van Bebber D, Murrenhoff H. Metal/carbon layers (ZrCg and HfCg) to reduce wear and friction in hydraulic components. In: Proceedings of the 3rd International Fluid Power Conference. Aachen: IFAS, 2002, 443–456
 11. Brizmer V, Kligerman Y, Etsion I. A laser surface textured parallel thrust bearing. *Tribology Transactions*, 2003, 46(3): 397–403
 12. Sharma S C, Yadav S K. Performance analysis of a fully textured hybrid circular thrust pad bearing system operating with non-Newtonian lubricant. *Tribology International*, 2014, 77: 50–64
 13. Fouflias D G, Charitopoulos A G, Papadopoulos C I, Kaitkis L, Fillon M. Performance comparison between textured, pocket, and tapered-land sector-pad thrust bearings using computational fluid dynamics thermohydrodynamic analysis. *Proceedings of the Institution of Mechanical Engineers, Part J: Journal of Engineering Tribology*, 2015, 229(4): 376–397
 14. Wang W, He Y Y, Zhao J, Li Y, Luo J B. Numerical optimization of the groove texture bottom profile for thrust bearings. *Tribology International*, 2017, 109: 69–77
 15. Filgueira Filho I C M, Bottene A C, Silva E J, Nicoletti R. Static behavior of plain journal bearings with textured journal—experimental analysis. *Tribology International*, 2021, 159: 106970
 16. Babu P V, Ismail S, Ben B S. Experimental and numerical studies of positive texture effect on friction reduction of sliding contact under mixed lubrication. *Proceedings of the Institution of Mechanical Engineers, Part J: Journal of Engineering Tribology*, 2021, 235(2): 360–375
 17. Etsion I, Halperin G. A laser surface textured hydrostatic mechanical seal. *Tribology Transactions*, 2002, 45(3): 430–434
 18. Brunetière N, Tournerie B. Numerical analysis of a surface-textured mechanical seal operating in mixed lubrication regime. *Tribology International*, 2012, 49: 80–89
 19. Wang X Y, Shi L P, Dai Q W, Huang W, Wang X L. Multi-objective optimization on dimple shapes for gas face seals. *Tribology International*, 2018, 123: 216–223
 20. Chacon R, Ivantsynova M. An investigation of the impact of micro surface on the cylinder block/valve plate interface performance. In: Proceedings of the 8th FPNI Ph.D Symposium on Fluid Power. Lappeenranta: ASME, 2014, V001T02A006
 21. Wang Z Q, Gu L Y, Li L. Experimental studies on the overall efficiency performance of axial piston motor with a laser surface textured valve plate. *Proceedings of the Institution of Mechanical Engineers, Part B: Journal of Engineering Manufacture*, 2013, 227(7): 1049–1056
 22. Wang Z Q, Hu S, Ji H, Wang Z, Liu X T. Analysis of lubricating characteristics of valve plate pair of a piston pump. *Tribology International*, 2018, 126: 49–64
 23. Chen Y, Zhang J H, Xu B, Chao Q, Liu G. Multi-objective optimization of micron-scale surface textures for the cylinder/valve plate interface in axial piston pumps. *Tribology International*, 2019, 138: 316–329
 24. Darbani A A, Shang L Z, Beale J R, Ivantsynova M. Slipper surface geometry optimization of the slipper/swashplate interface of swashplate-type axial piston machines. *International Journal of Fluid Power*, 2019, 20(2): 245–270
 25. Tang H S, Yin Y B, Li J. Lubrication characteristics analysis of slipper bearing in axial piston pump considering thermal effect. *Lubrication Science*, 2016, 28(2): 107–124
 26. Spencer N A. Design and development of a novel test method to measure the slipper/swashplate interface fluid film in a positive displacement machine. Dissertation for the Doctoral Degree. West Lafayette: Purdue University, 2014
 27. Zhang J H, Chao Q, Wang Q N, Xu B, Chen Y, Li Y. Experimental investigations of the slipper spin in an axial piston pump. *Measurement*, 2017, 102: 112–120
 28. Ransegnola T, Shang L Z, Vacca A. A study of piston and slipper spin in swashplate type axial piston machines. *Tribology International*, 2022, 167: 107420
 29. Murrenhoff H, Klocke F, Leonhard L, Derichs C. Mathematical modeling, optimization and production of microstructured contact surfaces for hydraulic displacement units—OptiKonS. Abschlussbericht zum gleichnamigen Forschungsprojekt. RWTH Aachen, 2010 (in German)
 30. Leonhard L, Murrenhoff H. Deterministic surface texturing for the tribologic contacts in hydrostatic machines. In: Proceedings of the 7th International Fluid Power Conference. Aachen: IFAS, 2010, 22–24
 31. Ye S G, Tang H S, Ren Y, Xiang J W. Study on the load-carrying capacity of surface textured slipper bearing of axial piston pump. *Applied Mathematical Modelling*, 2020, 77: 554–584
 32. Özmen Ö, Sinanoglu C, Caliskan A, Badem H. Prediction of leakage from an axial piston pump slipper with circular dimples using deep neural networks. *Chinese Journal of Mechanical Engineering*, 2020, 33(1): 28
 33. Pelosi M, Ivantsynova M. A novel thermal model for the piston/cylinder interface of piston machines. In: Proceedings of ASME 2009 Dynamic Systems and Control Conference. California: ASME, 2009, 37–44
 34. Yu T H, Sadeghi F. Groove effects on thrust washer lubrication. *Journal of Tribology*, 2001, 123(2): 295–304
 35. Zhang J H, Chen Y, Xu B, Chao Q, Zhu Y, Huang X C. Effect of surface texture on wear reduction of the tilting cylinder and the valve plate for a high-speed electro-hydrostatic actuator pump. *Wear*, 2018, 414–415: 68–78